Morphology-Dependent Performance of CuO Anodes via Facile and Controllable Synthesis for Lithium-Ion Batteries

Chen Wang,[†] Qing Li,[‡] Fangfang Wang,[†] Guofeng Xia,[†] Ruiqing Liu,[†] Deyu Li,[†] Ning Li,*[,†]
Jacob S. Spendelow,[‡] and Gang Wu*[,‡]

[†]School of Chemical Engineering and Technology, Harbin Institute of Technology, Harbin 150001, China
[‡]Materials Physics and Applications Division, Los Alamos National Laboratory, Los Alamos, New Mexico 87545, United States

Ⓢ *Supporting Information*

ABSTRACT: Nanostructured CuO anode materials with controllable morphologies have been successfully synthesized via a facile and environmentally friendly approach in the absence of any toxic surfactants or templates. In particular, leaf-like CuO, oatmeal-like CuO, and hollow-spherical CuO were obtained by changing the ligand agents. The structures and electrochemical performance of these as-prepared CuO were fully characterized by various techniques, and the properties were found to be strongly dependent on morphology. As anode materials for lithium-ion batteries, the leaf-like CuO and oatmeal-like CuO electrodes exhibit relatively high reversible capacities, whereas hollow-spherical CuO shows enhanced reversible capacity after initial degradation. Furthermore, an excellent high rate capability was obtained for the leaf-like CuO and hollow-spherical CuO electrodes. These results may provide valuable insights for the development of nanostructured anodes for next-generation high-performance lithium-ion batteries.

KEYWORDS: *copper oxide, morphology dependence, electrochemical performance, anode materials, lithium-ion batteries*
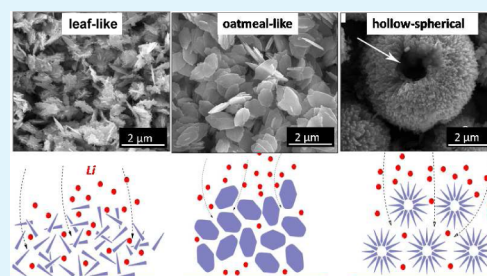
1. INTRODUCTION

Transition-metal oxides (M_xO_y, M = Fe, Co, Ni, Mn, Cu, etc.) are promising anode materials for lithium-ion batteries (LIBs). These materials can react with lithium based on the reduction/oxidation reaction mechanism of $M_xO_y + 2yLi = yLi_2O + xM$, which exhibits large rechargeable capacities.[1−6] Among these transition-metal oxides, copper oxide (CuO) is of particular interest for its inexpensiveness, good safety, large theoretical capacity (670 mAh g^{-1}), and low toxicity.[7−9] However, CuO is a semiconductor with low electrical conductivity, which is unfavorable for charge transfer. In addition, CuO-based electrodes suffer from significant volume expansion and dispersion of Cu particles in the Li_2O matrix during discharge−charge processes, which leads to severe mechanical strain and rapid capacity decay.[10,11]

Improved electrochemical performance of CuO-based anodes is required to meet the needs of next-generation LIBs. Tremendous efforts have been devoted to improving the performance of CuO-based electrodes through nanostructured design, morphology control techniques, and hybridization of composite materials, resulting in materials with encouraging electrochemical properties and unique structures.[7,12,13] For instance, CuO electrodes containing urchin-like particles were reported to deliver an electrochemical capacity above 560 mAh g^{-1} after 50 cycles at a 150 mA g^{-1} rate.[14] 3D dendrite-shaped CuO hollow micro/nanostructures show enhanced performance.[15] A type of hierarchical micro/nanostructured electrode was developed by fabricating $Cu(OH)_2$ using a facile NH_3

corrosion approach, yielding a structure with an excellent cycling stability of 651.6 mAh g^{-1} after 100 cycles at a 0.5 C rate, and a high-rate capability of 561.6 mAh g^{-1} at a 10 C rate.[16]

All of these techniques have been demonstrated as promising ways to fabricate CuO anode materials. However, the requirement of toxic raw materials, the expense of removing the template, and contamination by byproducts have limited large-scale applications.[12] Thus, new synthetic strategies for fabricating CuO, especially via simple and environmentally friendly processes without surfactants or templates, are highly desired.[17−19] The use of nontoxic chemical agents as templates, chelating agents, or reactants represents a possible pathway to greener and lower-cost synthesis of CuO anodes. Examples of such chemicals include malic acid, sodium citrate, and urea. Malic acid is a green organic material that is often used as an additive agent in foods and pharmaceuticals.[20] Malic acid is also used as a chelating agent in electroplating and electroless plating due to its high ability for complexation of copper ions in solution.[21,22] Sodium citrate is another example of a low-toxicity material that is commonly used as a chelator as well as a food additive.[23] As a normal waste product of human metabolic processes with low toxicity, urea is one of the simplest organic compounds, which is employed as a ligand and ammonia

source during the hydrothermal synthesis process of structured metal oxides.[24,25]

In this work, leaf-like CuO, oatmeal-like CuO, and hollow-spherical CuO nanostructures with controllable morphologies were developed via a simple, green, and cost-effective method suitable for large-scale synthesis. Malic acid, sodium citrate, and urea were employed as ligands to control the synthesis of CuO nanostructures. In electrochemical measurements, the leaf-like CuO and oatmeal-like CuO nanostructured electrodes exhibit high reversible capacities, whereas hollow-spherical CuO possesses enhanced reversible capacity after 55 cycles.

2. EXPERIMENTAL SECTION

2.1. Materials Synthesis. All reagents were analytical grade and used without further purification. As for the synthesis of leaf-like CuO, 3.02 g of cupric nitrate and 2.51 g of DL-malic acid were dissolved in 300 mL of deionized water with vigorous stirring for 30 min, followed by addition of 200 mL of 1.25 M sodium hydroxide aqueous solution under continuous vigorous stirring. The mixture was maintained under constant stirring at 90 °C for over 2 h in a water bath. The as-formed precipitate was collected and washed several times with deionized water and ethanol by centrifugation, and then dried in a vacuum oven at 75 °C for 12 h (denoted as leaf-like CuO before calcination). The as-synthesized intermediate product was subsequently calcined in air at 400 °C for 2 h, yielding a black CuO powder (denoted as leaf-like CuO after calcination).

The synthesis procedure of the oatmeal-like CuO was the same as that of the leaf-like but using 3.02 g of cupric nitrate and 3.68 g of sodium citrate. As for the synthesis of hollow-spherical CuO, 1.16 g of cupric nitrate and 0.86 g of urea were dissolved in 320 mL of deionized water with vigorous stirring, and then the solution was transferred into a 400 mL Teflon-lined stainless steel autoclave, followed by a hydrothermal treatment at 180 °C for 18 h. After allowing the mixture to cool to room temperature, the as-formed precipitate was collected and washed several times with deionized water and ethanol, and then dried in a vacuum oven at 75 °C for 12 h (denoted as hollow-spherical CuO before calcination). The as-synthesized intermediate product was further calcined in air at 400 °C for 2 h, denoted as hollow-spherical CuO after calcination.

2.2. Physical Characterization. The structure determination was carried out by using X-ray diffraction (XRD, D/MAX-RB, Rigaku, Japan) with Cu Kα (1.50598 Å) radiation at 40 kV and 200 mA. The XRD pattern was recorded in the 2θ range of 20–70°. The morphology and microstructure of the samples were characterized using a field-emission scanning electron microscope (FE-SEM, Quanta 200F, FEI, USA) with an accelerating voltage of 30.00 kV. Atomic concentration and chemical bonding information were obtained from the specimen surfaces by X-ray photoelectron spectroscopy (XPS, Thermo Scientific K-Alpha, Thermo Fisher Scientific, USA). The instrument was equipped with a monochromatic Al Kα X-ray source. Spectra were collected using an X-ray spot size of 400 μm.

2.3. Electrochemical Measurements. The electrochemical characterization was performed with CR2025-type coin cells containing the CuO working electrode. The working electrodes were prepared by a slurry coating method with 80 wt % of sample, 10 wt % acetylene black, and 10 wt % polyvinylidene fluoride (PVDF) binder dispersed in N-methyl-2-pyrrolidone (NMP). The mass of each CuO thin electrode was precisely measured with a microbalance before coin cell assembly. Coin cells were assembled in an argon-filled glove box with a metallic lithium foil as the combined reference and counter electrodes. The moisture content and oxygen level in the glove box were maintained less than 1 ppm. The electrolyte was 1 M LiPF$_6$ in a 1:1 (v/v) mixture of ethylene carbonate (EC) and dimethyl carbonate (DMC) with Celgard 2300 polypropylene as separator.[26] The cells were galvanostatically charged and discharged at a constant current density of 0.1 C (1 C = 670 mAh g^{-1}) based on the weight of the CuO sample on a battery test system (Arbin 2000-BT) for galvanostatic discharge–charge cycling tests. Cyclic voltammetry (CV) was conducted on an electrochemical workstation (CHI-760d) at a scan rate of 0.2 mV s^{-1} from 0.02 to 3.0 V. Electrochemical impedance spectroscopy (EIS) was also performed using an electrochemical workstation (PAR 2573). The frequency of EIS ranged from 100 kHz to 0.01 Hz at the open-circuit potential.

3. RESULTS AND DISCUSSION

3.1. XRD Patterns. The phase purity of the as-prepared samples (leaf-like CuO, oatmeal-like CuO, and hollow-spherical CuO before and after calcination) was determined by XRD as shown in Figure 1. All the diffraction peaks can be readily
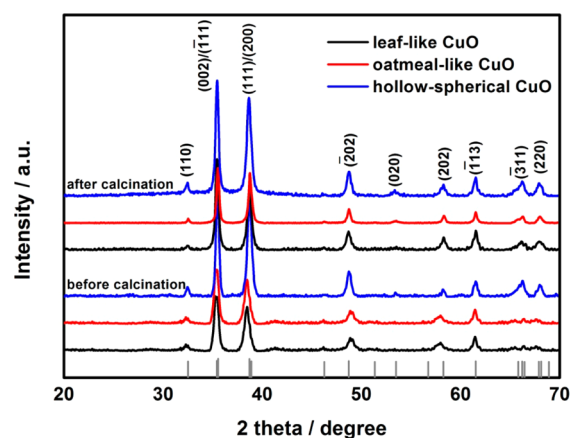

Figure 1. XRD patterns of the leaf-like CuO, oatmeal-like CuO, and hollow-spherical CuO samples before and after calcination.

indexed to the monoclinic symmetry of CuO (space group $C2/c$, a = 4.684 Å, b = 3.425 Å, c = 5.129 Å, β = 99.47°, JCPDS file no. 45-0937). No obvious impurities were detected, indicating the high phase purity of the as-prepared samples. The broadening of all the recorded peaks in the XRD pattern indicates that the crystallites are small. Average crystallite size of the leaf-like CuO, oatmeal-like CuO, and hollow-spherical CuO after calcination was determined to be 22.1, 26.7, and 23.8 nm, respectively, by using the Scherrer formula. The leaf-like CuO and hollow-spherical CuO exhibit similar broad XRD lines, which are different from those of the oatmeal-like CuO.

3.2. XPS Analysis. The leaf-like CuO nanostructures were characterized by XPS. The XPS survey scans of as-prepared CuO samples before and after calcination are shown in Figure 2a for comparison. The C 1s peaks were corrected to be 284.6 eV; all the other peaks were corrected accordingly. The survey scan spectra of both samples demonstrate the exclusive presence of Cu, O, and C elements, corroborating the high purity of the samples. In Figure 2b, a subtle decrease in binding energy has been observed in the main Cu 2p$_{3/2}$ and Cu 2p$_{1/2}$ lines after calcination, which could be attributed to the change of surface chemical composition after the calcination process.[27] The difference between spin−orbit coupling energy of as-prepared samples for Cu 2p$_{3/2}$ and Cu 2p$_{1/2}$ is ca. 20 eV, which is in agreement with the +2 copper oxidation state feature.[28]

Cu 2p core-level spectra of CuO samples before and after calcination were resolved using Gaussian curve-fitting analysis and are presented in Figure 2c,e, respectively. Before calcination, the main Cu 2p$_{3/2}$ peak presents two components. The main one is located at 937.7 eV, which is identified as Cu^{2+} characteristic of the Cu(OH)$_2$ phase. Detected Cu(OH)$_2$ could be attributed to the presence of residual OH$^-$ groups on the surface of CuO before calcination. The other one located at
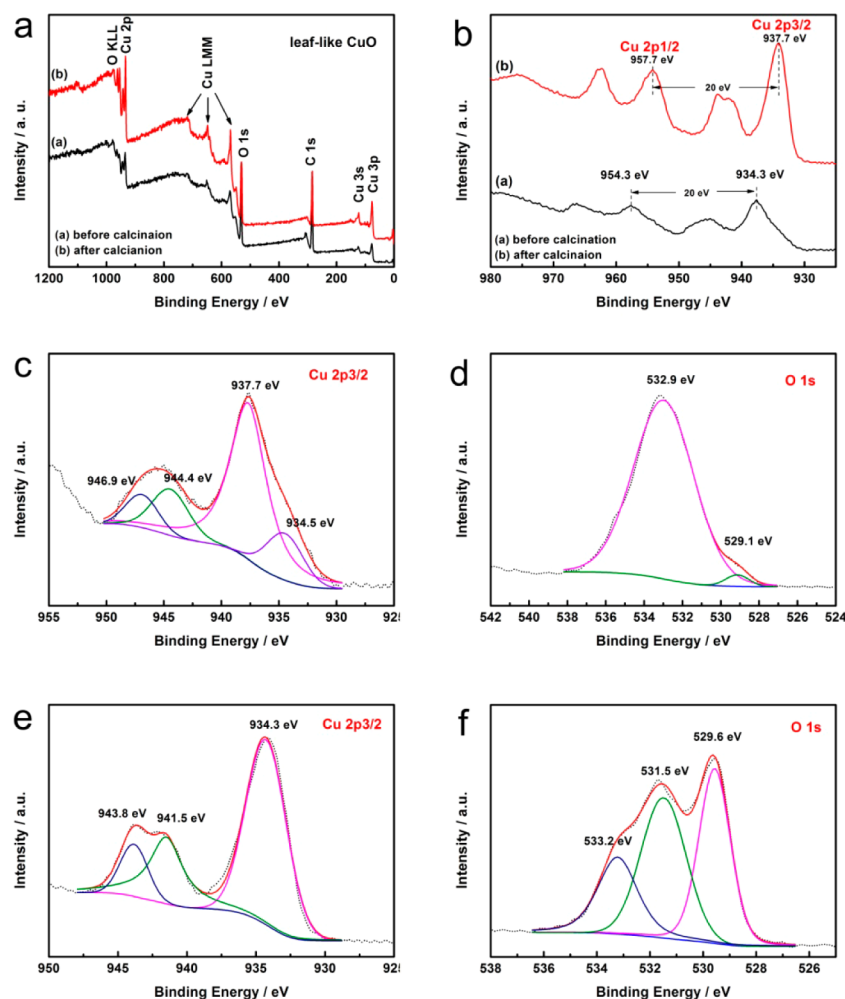
Figure 2. XPS spectra of the leaf-like CuO: (a, b) survey spectra; (c, d) curve-fitting spectra of Cu $2p_{3/2}$ and O 1s before calcination and (e, f) after calcination.
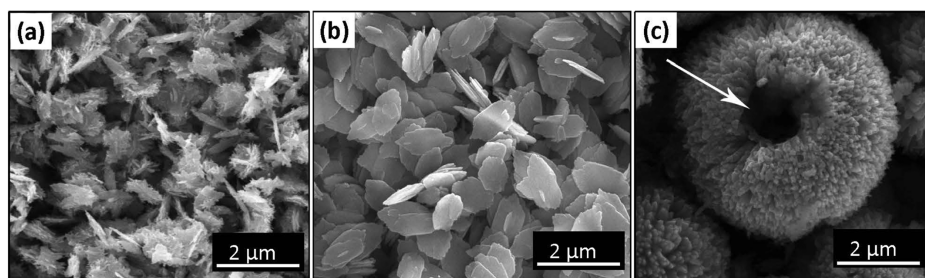

Figure 3. SEM images of the (a) leaf-like CuO, (b) oatmeal-like CuO, and (c) hollow-spherical CuO samples after calcination.

934.5 eV can be assigned to Cu^{2+} characteristic in the CuO phase.[29−31] Moreover, the peaks at 944.4 and 946.9 eV are assigned to Cu^{2+} satellite peaks, attesting that $Cu(OH)_2$ is the main component on the surface of the sample before calcination.[17] In contrast, the Cu $2p_{3/2}$ peak in Figure 2e exhibits only one component located at 934.3 eV, along with two satellite peaks at 941.5 and 943.8 eV. These features correspond to a Cu^{2+} state in CuO, suggesting that calcination is a key to forming CuO.

The O 1s core-level XPS spectra of CuO samples before and after calcination were also resolved using a curve-fitting procedure and are displayed in Figure 2d,f, respectively. Before calcination, the main O 1s peak observed at 532.9 eV

corresponds to $Cu(OH)_2$. A relatively weak peak is also observed with a lower binding energy value at 529.1 eV, which is attributed to the presence of CuO on the surface of the sample.[31,32] After calcination, the main peak observed at 529.6 eV corresponds to the binding energy value of CuO and the other peaks (531.5 and 533.2 eV) may originate from oxygen and moisture in air adsorbed on the CuO surface.[30,33,34]

After a calcination treatment, the Cu $2p_{3/2}$ and O 1s XPS spectra observed with the oatmeal-like CuO (Figure S1a,b, Supporting Information) and the hollow-spherical CuO (Figure S1c,d, Supporting Information) exhibit similar features with those of the leaf-like CuO, suggesting the predominant existence of Cu^{2+} in CuO samples after calcination.

3.3. Morphology. Figure S2a (Supporting Information) and Figure 3a show the typical SEM images of the as-prepared leaf-like CuO nanostructure samples before and after calcination. Before calcination (Figure S2a), CuO exhibits a leaf-like morphology, and the leaf-like architectures are well maintained after calcination, as presented in Figure 3a. The image of a typical leaf-like cluster shows that it is composed of nanoribbons of a few nanometers in thickness, about 100−150 nm wide, and about 1.3−2.0 μm long, which grow out from the two sides of the main base nanorod and coexist with it in the same plane.

The CuO produced using sodium citrate displays an oatmeal-like morphology (Figure 3b and Figure S3, Supporting Information) consisting of platelets with a width of about 0.6−0.75 μm and a length of about 1.2−1.5 μm. These results demonstrate that the nature of the ligand is a key factor in determining the morphology of CuO particles, which might be related to differences in coordination ability, steric effects, interaction with copper ion, etc.

Urea was also employed as a ligand to control the morphology, resulting in hollow-spherical CuO particles that are composed of numerous nanorods, as displayed in Figure 3c and Figure S4 (Supporting Information). The time-dependent evolution process was monitored by SEM images to provide insights into the growth of CuO hollow microspheres. In Figure S4a (Supporting Information), solid spheres with a diameter of 4.5−6.5 μm were formed after 6 h of reaction. When the reaction time was extended to 12 h, the surfaces of the spheres became rougher (Figure S4b, Supporting Information). Further extending the reaction time up to 18 h made the surface of CuO spheres much rougher than before, as shown in Figure S4c, and causes the nanorod-aggregate nature of the spheres to become more apparent (Figure S4d) (Supporting Information). The SEM image of a broken sphere clearly reveals the hollow inner structure (white arrow in Figure S4e, Supporting Information). An SEM image of hollow-spherical CuO after 18 h reaction time and subsequent calcination is displayed in Figure 3c, demonstrating that the CuO microspheres maintained their spherical morphology and rough surfaces after the heat treatment.

3.4. CV Measurements. The electrochemical behavior of the as-prepared CuO samples after calcination was examined by CV in Figure 4. In the first cathodic scan process (lithiation process), three cathodic peaks in the potential range of 0.02−3.0 V are observed similarly for three as-prepared CuO samples at 1.65 V (weak), 0.96 V (strong), and 0.76 V (medium). Indeed, there are several complex phases that are formed at different potentials during the first cathodic scan process, accompanied with the destruction−rebuilding of the electrode microstructure.[1,4] In particular, the most possible lithium reactions are associated with the oxygen extraction from CuO and the formation of Li_2O as a separate phase. Thus, the overall electrochemical reaction was proposed (below), which has been verified by Débart et al. using the potentiodynamic intermittent titration technique (PITT), in situ XRD, and transmission electron microscope (TEM) measurements efficiently.[1]

$$CuO + 2Li^+ + 2e^- \leftrightarrow Cu^0 + Li_2O \qquad (1)$$
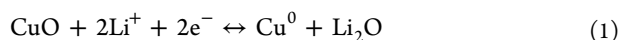
Especially, at least three main electrochemical steps were identified.[4,16,35] During the reduction, the formation of an intermediate ($Cu_{1-x}^{II}Cu_x^{I}O_{1-x/2}$) was involved.[1,4,36]
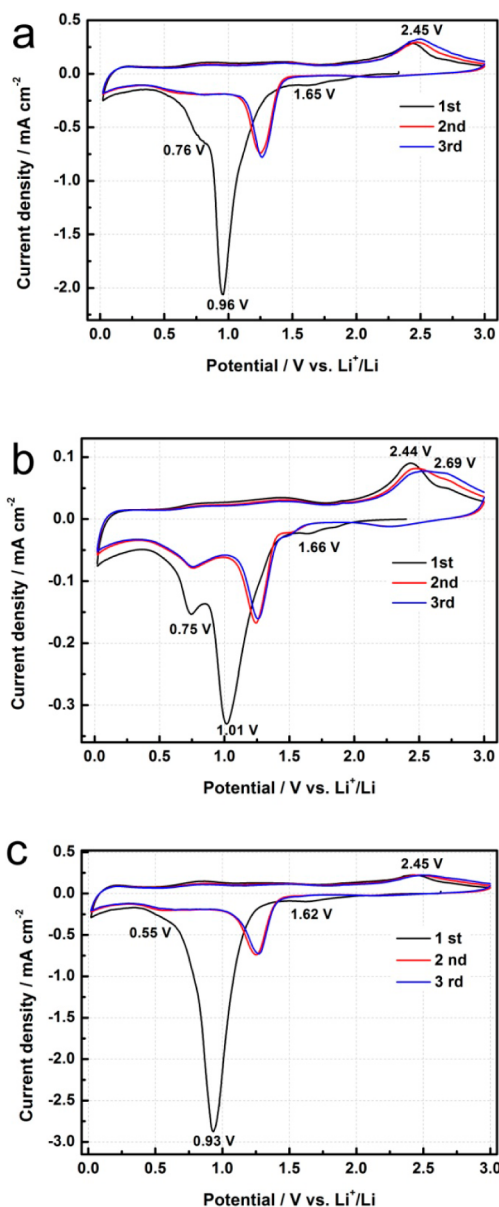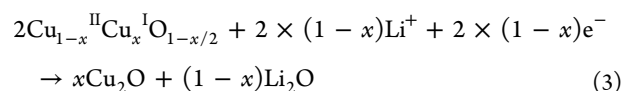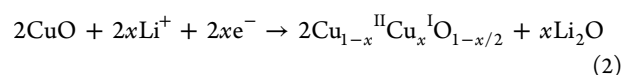

Figure 4. Cyclic voltammograms of the calcined (a) leaf-like CuO, (b) oatmeal-like CuO, and (c) hollow-spherical CuO from 3.0 to 0.02 V (vs Li$^+$/Li) at a scan rate of 0.2 mV s^{-1}.

$$2CuO + 2xLi^+ + 2xe^- \rightarrow 2Cu_{1-x}^{II}Cu_x^{I}O_{1-x/2} + xLi_2O \qquad (2)$$

$$2Cu_{1-x}^{II}Cu_x^{I}O_{1-x/2} + 2 \times (1-x)Li^+ + 2 \times (1-x)e^-$$
$$\rightarrow xCu_2O + (1-x)Li_2O \qquad (3)$$

The insertion of a limited amount of Li (0.4Li/CuO) is expected at a high potential (1.65 V), involving a formation of solid-solution $Cu_{1-x}^{II}Cu_x^{I}O_{1-x/2}$ (Reaction 2). Then the lithiation process is accompanied with another electrochemical reaction around 0.96 V associated with a phase transformation from $Cu_{1-x}^{II}Cu_x^{I}O_{1-x/2}$ into the Cu_2O phase (Reaction 3). Thus, the reduction of Cu^{2+} to Cu^+ requires two distinct electrochemical reactions that correspond to two different potentials.[1,10,32]

Further decomposition of Cu_2O into Cu and Li_2O is expected at a potential 0.76 V.[4,37]

$$Cu_2O + 2Li^+ + 2e^- \rightarrow 2Cu + Li_2O \qquad (4)$$
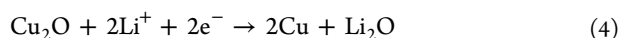
In addition, partial irreversible electrolyte decomposition and the consequent growth of a solid electrolyte interface (SEI) layer also take place in the more negative potential region.[2,4]

Although all of the as-prepared CuO electrodes exhibit three reduction peaks at similar potentials, it is noteworthy that oatmeal-like CuO exhibits one comparatively strong cathodic peak (located at about 0.75 V) during the cathodic scan process, which is different from that of other as-prepared CuO samples in Figure 4. This cathodic peak is associated with the structural destruction and subsequent transformation from Cu_2O into Cu^0 particles and amorphous Li_2O, and also includes partial formation of the SEI layer.[38] In other words, this step mainly involves frequent particle structural destruction—rebuilding and repetitive formation of the SEI layer for oatmeal-like CuO, which could weaken the connection between the catalytic sites and the current collector and give rise to poor cycle performance and poor rate performance. In contrast, in Figure 4a,c, both the leaf-like CuO and the hollow-spherical CuO exhibit relatively broad and weak peaks in this potential region, which may be favorable to cyclability.

In the first anodic scan process (delithiation process), one broad oxidation peak is found at 2.45 V for three as-prepared CuO samples, mainly corresponding to the formation of Cu_2O. However, a distinctive anodic peak at 2.69 V was observed with the oatmeal-like CuO (Figure 4b), which is different from the leaf-like CuO and the hollow-spherical CuO, attributed to partial oxidation of Cu_2O into CuO.[4] This obvious phase change during cycling may also cause damage associated with volume change, and decreasing cycle life. In addition, there is an extra broad peak from 0.7 to 2.0 V in the positive scan, which could be attributed to partial decomposition of the SEI layer in the oatmeal-like CuO.

During subsequent cycles, all cathodic and anodic peaks of as-prepared CuO electrodes are found to shift slightly to higher potentials with very good reproducibility, suggesting an excellent reversibility for the redox reaction.

For comparison, CV curves of CuO before calcination are also provided in Figure S5 (Supporting Information). As mentioned in the literature,[39] the remnant hydroxyl groups could reduce the stability of the SEI layer and lead to rapid capacity loss. Meanwhile, calcination was proven to be an effective and feasible process for removing hydroxyl groups, as discussed above in the XPS spectra. Comparing CV curves in Figure 4 and Figure S5, calcination may improve the cycling performance, and facilitate Cu_xO structural transformations.

To compare the conductivity of the as-prepared nano-structured CuO electrodes, EIS was carried out as shown in Figure 5a. An equivalent circuit model as shown in Figure 5b especially for the oxide anode was employed to simulate these spectra.[40]

In the EIS equivalent circuit, R_e in the high frequency region is related to the Ohmic resistance; R_f in the circuit corresponds to the Ohmic resistances of Li^+ migration through the SEI film. C_f is related to passivation film capacitance, and the Q constant phase element (CPE) accounts for the double-layer capacitance. R_{ct} is the charge-transfer resistance of corresponding electrochemical reactions, and Z_W at low frequencies represents the Warburg impedance related to lithium-ion diffusion. Generally, the semicircle in the high–middle frequency region is related to Li diffusion occurring at the electrode/electrolyte interface through the SEI film, whereas the middle frequency
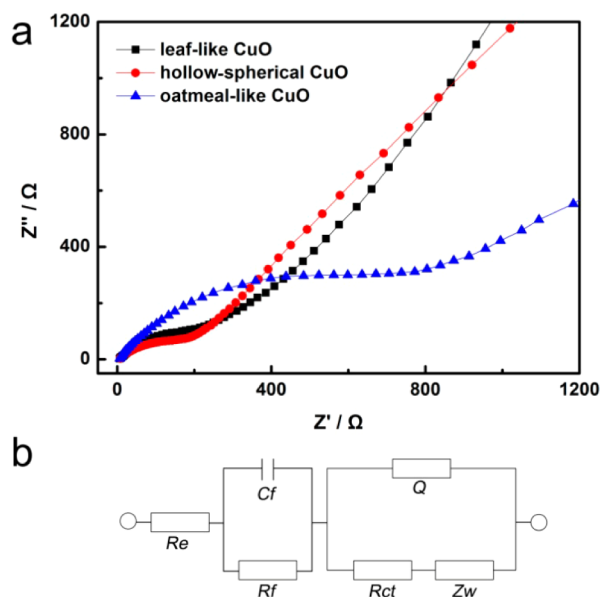

Figure 5. (a) Nyquist plots of as-prepared CuO samples with different morphologies. (b) The equivalent circuit model used to simulate the spectra.

range of the semicircle corresponds to the charge-transfer process, and the straight line in the low frequency region can be attributed to Warburg impedance.[41,42]

The simulated values for R_e, R_f, R_{ct}, and R_Σ are summarized in Table 1. It can be seen that the values of R_e for the three

Table 1. Simulated Parameters of EIS Using the Equivalent Circuit for CuO Samples with Different Morphologies

samples	$R_e/[\Omega]$	$R_f/[\Omega]$	$R_{ct}/[\Omega]$	$R_\Sigma/[\Omega]$
leaf-like	4.7	45.7	206.2	256.6
oatmeal-like	5.3	321.1	291.1	617.8
hollow-spherical	5.2	43.8	171.7	220.7

CuO samples are similar. There is no significant difference of R_f and R_{ct} between the leaf-like CuO and the hollow-spherical CuO. However, the R_f value of the oatmeal-like CuO is significantly larger than those of other samples. Furthermore, the value of total resistance of the oatmeal CuO is the largest. It looks like the results of impedance are in good agreement with the electrochemical performance discussed below, and a conclusion can be deduced that the resistance of the SEI film is the main reason for the inferior electrochemical performance observed with the oatmeal-like CuO anodes.

3.5. Battery and Electrochemical Measurements. Figure 6 reveals the galvanostatic discharge–charge curves of various CuO samples after calcination for the 1st, 2nd, 3rd, and 15th cycles recorded at a 0.1 C rate. The multiple plateaus in the charge curves demonstrate that multiple reactions take place during the conversion reactions between CuO and lithium. This observation is consistent with the CV curves above, which exhibit multiple reduction peaks. The initial charge and discharge capacities of the leaf-like CuO are measured to be 1002.4 and 563.8 mAh g^{-1}, respectively. An irreversible capacity loss in the first charge–discharge cycle should be mainly attributed to electrolyte decomposition and formation of SEI layers. Afterwards, reversible capacities are
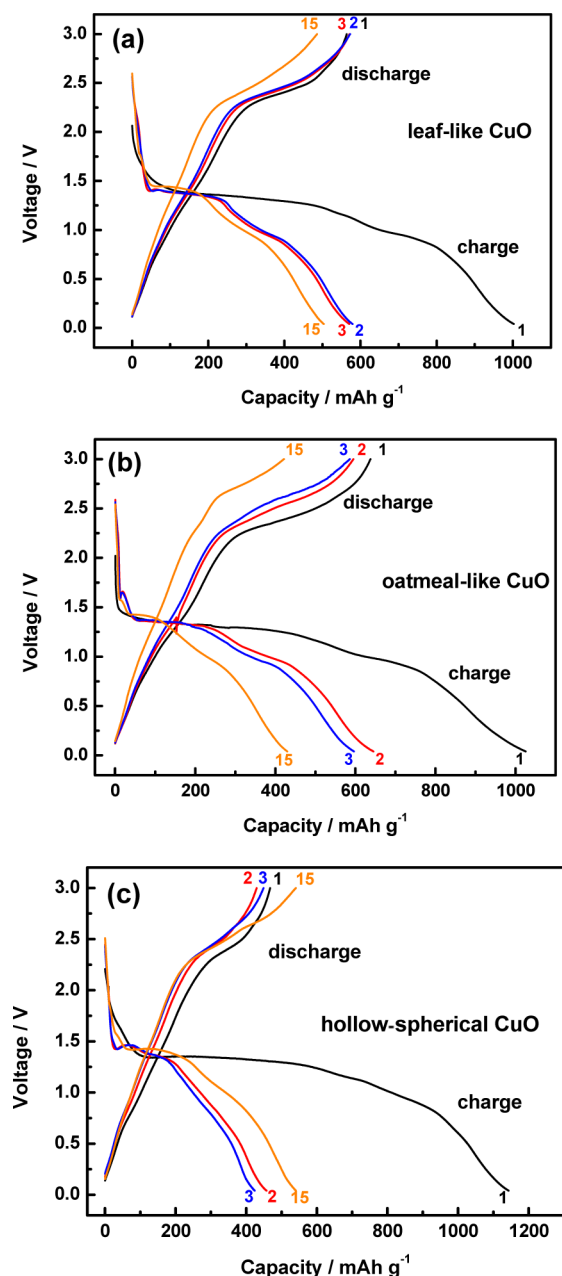
1247

dx.doi.org/10.1021/am405061c | ACS Appl. Mater. Interfaces 2014, 6, 1243–1250

Figure 6. Charge−discharge curves (1st, 2nd, 3rd, and 15th) of the (a) leaf-like CuO, (b) oatmeal-like CuO, and (c) hollow-spherical CuO after calcination.

nearly constant, attesting to the improved contact between the electrode and the electrolyte, and the increased SEI layer.[43]

The cycling performance of the as-prepared leaf-like CuO electrode, measured between 0.04 and 3.0 V at a current density of 0.1 C, is shown in Figure 7a. From the second cycle onwards, the leaf-like CuO electrode exhibits excellent cyclic capacity retention, with a stable capacity of about 563.8 mAh g^{-1}, and the Coulombic efficiency is generally nearly 98%. It is believed that the excellent capacity of the leaf-like CuO electrode mainly originates from its proper nanostructure, which provides short diffusion paths both for electrons and lithium ions at the electrode/electrolyte junction.[44] After 55 cycles, the reversible capacity of CuO after calcination is still as high as 421.0 mAh g^{-1}, indicating high cyclic stability. In contrast, the CuO before calcination exhibits much faster

performance decay and lower capacity after 55 cycles, probably due to the existence of $Cu(OH)_2$ impurities on the sample surface, as demonstrated by XPS above. The good crystallinity (Figure 1a) and the purity of the CuO surface (Figure 2) are believed to be of great importance to the discharge−charge performance of CuO nanomaterials and the stable SEI layer on the surface.

As for the oatmeal-like CuO sample (Figure 7c), the electrode exhibits a reversible discharge capacity of 231.9 mAh g^{-1} after 55 cycles and the Coulombic efficiency exhibits large fluctuation after the second cycle. Interestingly, after 55 cycles, the reversible capacity of hollow-spherical CuO is significantly enhanced from 467.7 to 543.9 mAh g^{-1}, with a good Coulombic efficiency (Figure 7e). At the beginning of the cycle test, the interiors of the hollow-spherical CuO are probably not in good contact with the electrolyte and the build-up of the SEI layer may need a number of cycles.[45] That may explain the increasing cycle capacity of hollow-spherical CuO with cycle numbers. Also, the performance of hollow-spherical CuO after calcination is superior to that of the sample before calcination. The possible reasons are the same as discussed above.

Figure 7b,d,f exhibits the rate capability of three CuO electrodes at different current densities. Overall, the leaf-like CuO and the hollow-spherical CuO show good rate capability performance. Upon decreasing the rate to 0.1 C, the reversible capacities of the leaf-like CuO and the hollow-spherical CuO reached 677.1 and 648.8 mAh g^{-1}, respectively, which may result from a better exchange capacity between CuO/ electrolyte and the growth of the polymer layer on the surface after a number of cycles.[45] In contrast, the capacity of oatmeal-like CuO decreased gradually when the rate was decreased to 0.1 C after 55 cycles. Different to 3D structures of the leaf- and hollow-spherical CuO anodes, the oatmeal-like CuO particles with a smaller size is kind of a 2D morphology. This type of structure has a lack of order, possibly hindering Li ion diffusion in the formed SEI films, evidenced by the high R_f determined from EIS (Table 1). In addition, increased contact resistance among particles could be speculated, resulting in a slow lithium-ion diffusion on the oatmeal-like structure.

On the basis of our experimental results, morphology seems to be a key factor to control electrochemical performance. However, different structure parameters will affect different electrochemical metrics (specific capacity, cycle stability, and rate performance). In particular, the leaf-like CuO and the hollow-spherical CuO show decent electrochemical properties. Thanks to the unique leaf-like CuO nanostructures, the electrolyte may be able to fully penetrate the electrode, leading to a higher CuO/electrolyte contact area and more facile lithium-ion transport in the electrolyte within the cavity space, especially at high current density. However, the reversible capacities of the leaf-like CuO and the oatmeal-like CuO are found to be decreased during cycling. In contrast, the increase in reversible capacity of the hollow-spherical CuO during cycling might be related to the unique structure of these hollow spheres. Specifically, the nanorod building blocks and the hollow interiors may provide efficient transport of lithium ions because of the short diffusion length and the high porosity, thereby mitigating the performance loss. Furthermore, the appropriate void space between nanorods could serve as an effective elastic buffer to relieve the volume expansion during lithium-ion uptake/release as well as the strain accumulated in the CuO particles.
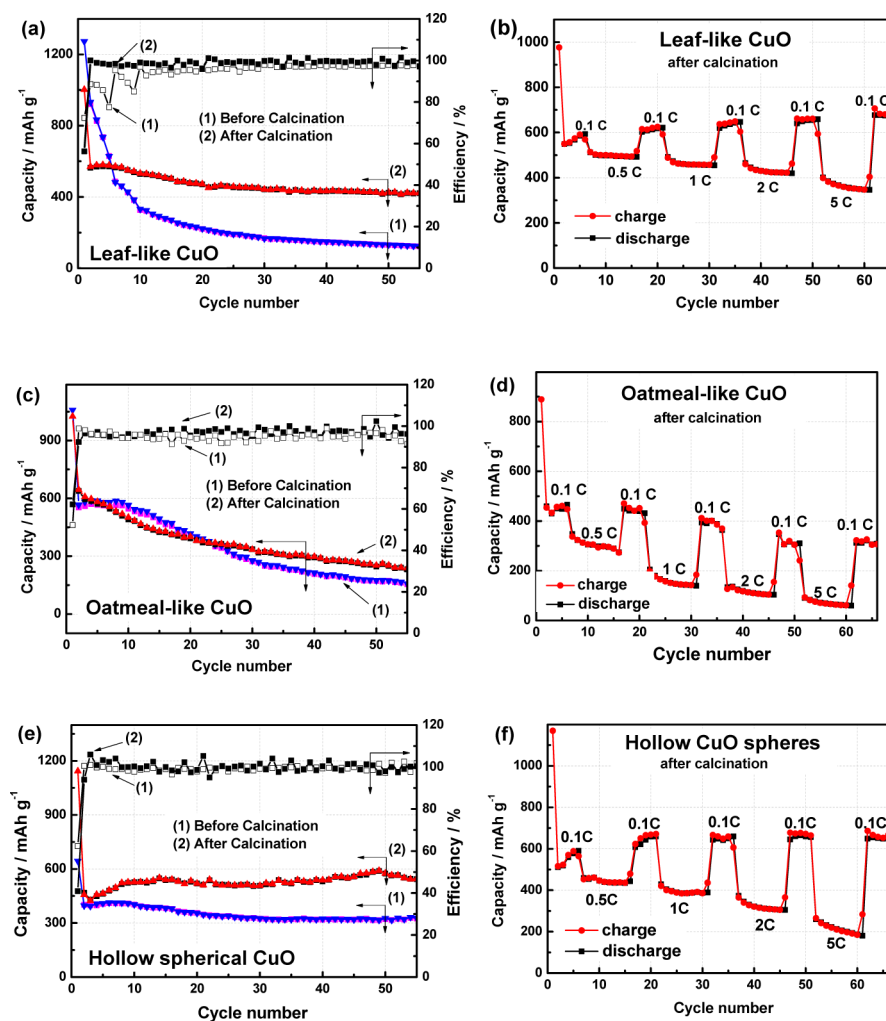
Figure 7. Cycling performance and Coulombic efficiency at a 0.1 C rate of (a) the leaf-like CuO, (c) the oatmeal-like CuO, and (e) the hollow-spherical CuO. Rate performance for (b) the leaf-like CuO, (d) the oatmeal-like CuO, and (f) the hollow-spherical CuO anodes after calcinations.

4. CONCLUSIONS

In this work, the effect of CuO anode morphologies on lithium-ion battery performance is systematically investigated. Leaf-like CuO, oatmeal-like CuO, and hollow-spherical CuO particles with a controllable structure and uniform size were successfully synthesized via a green and facile approach. When they are used as anode materials for LIBs, the leaf-like CuO and oatmeal-like CuO electrodes show relatively high initial reversible capacities (563.8 and 637.7 mAh g^{-1}, respectively); the hollow-spherical CuO electrode demonstrates an improved cycling stability with a reversible capacity increasing from 467.7 to 543.9 mAh g^{-1} after 55 cycles, as well as good Coulombic efficiency. Good rate capability is also observed with the leaf-like CuO and hollow-spherical CuO anodes. The excellent performance is likely related to the novel CuO nanostructures with plenty of voids, which are able to shorten the lithium-ion diffusion length and buffer the volume change during the discharge−charge process. The facile synthetic methods of producing advanced CuO nanostructures demonstrated in this study, as well as the excellent electrochemical performance of these materials, make them promising candidates for application as anode materials in next-generation high-performance LIBs.

■ ASSOCIATED CONTENT

Ⓢ Supporting Information

Less-essential physical and electrochemical characterization is presented in the Supporting Information. This material is available free of charge via the Internet at http://pubs.acs.org.

■ AUTHOR INFORMATION

Corresponding Authors

*E-mail: wugang@lanl.gov. Phone: 505-665-0659 (G.W.).
*E-mail: lininghit@263.net. Phone: +86-451-86413721 (N.L.).

Notes

The authors declare no competing financial interest.

■ ACKNOWLEDGMENTS

■ REFERENCES

(1) Débart, A.; Dupont, L.; Poizot, P.; Leriche, J. B.; Tarascon, J. M. *J. Electrochem. Soc.* **2001**, *148*, A1266−A1274.

(2) Sahay, R.; Suresh Kumar, P.; Aravindan, V.; Sundaramurthy, J.; Chui Ling, W.; Mhaisalkar, S. G.; Ramakrishna, S.; Madhavi, S. *J. Phys. Chem. C* **2012**, *116*, 18087−18092.

(3) Xiang, J. Y.; Wang, X. L.; Xia, X. H.; Zhang, L.; Zhou, Y.; Shi, S. J.; Tu, J. P. *Electrochim. Acta* **2010**, *55*, 4921−4925.

(4) Wang, S. Q.; Zhang, J. Y.; Chen, C. H. *Scr. Mater.* **2007**, *57*, 337−340.

(5) Xia, G.; Li, N.; Li, D.; Liu, R.; Wang, C.; Li, Q.; Lu, X.; Spendelow, J. S.; Zhang, J.; Wu, G. *ACS Appl. Mater. Interfaces* **2013**, *5*, 8607−8614.

(6) Liu, R.; Li, N.; Xia, G.; Li, D.; Wang, C.; Xiao, N.; Tian, D.; Wu, G. *Mater. Lett.* **2013**, *93*, 243−246.

(7) Zhang, W.; Li, M.; Wang, Q.; Chen, G.; Kong, M.; Yang, Z.; Mann, S. *Adv. Funct. Mater.* **2011**, *21*, 3516−3523.

(8) Volanti, D. P.; Orlandi, M. O.; Andrés, J.; Longo, E. *CrystEngComm* **2010**, *12*, 1696−1699.

(9) Wang, L.; Cheng, W.; Gong, H.; Wang, C.; Wang, D.; Tang, K.; Qian, Y. *J. Mater. Chem.* **2012**, *22*, 11297−11302.

(10) Yang, Z.; Wang, D.; Li, F.; Liu, D.; Wang, P.; Li, X.; Yue, H.; Peng, S.; He, D. *Mater. Lett.* **2013**, *90*, 4−7.

(11) Chen, X.; Zhang, N. Q.; Sun, K. N. *J. Phys. Chem. C* **2012**, *116*, 21224−21231.

(12) Guan, X.; Li, L.; Li, G.; Fu, Z.; Zheng, J.; Yan, T. *J. Alloys Compd.* **2011**, *509*, 3367−3374.

(13) Xu, M.; Wang, F.; Ding, B.; Song, X.; Fang, J. *RSC Adv.* **2012**, *2*, 2240−2243.

(14) Park, J. C.; Kim, J.; Kwon, H.; Song, H. *Adv. Mater.* **2009**, *21*, 803−807.

(15) Hu, Y.; Huang, X.; Wang, K.; Liu, J.; Jiang, J.; Ding, R.; Ji, X.; Li, X. *J. Solid State Chem.* **2010**, *183*, 662−667.

(16) Chen, X.; Zhang, N.; Sun, K. *J. Mater. Chem.* **2012**, *22*, 13637−13642.

(17) Gao, S.; Yang, S.; Shu, J.; Zhang, S.; Li, Z.; Jiang, K. *J. Phys. Chem. C* **2008**, *112*, 19324−19328.

(18) Cao, H.; Liang, R.; Qian, D.; Shao, J.; Qu, M. *J. Phys. Chem. C* **2011**, *115*, 24688−24695.

(19) Zhang, J.; Sun, Y.; Yao, Y.; Huang, T.; Yu, A. *J. Power Sources* **2013**, *222*, 59−65.

(20) Goldberg, I.; Rokem, J. S.; Pines, O. *J. Chem. Technol. Biotechnol.* **2006**, *81*, 1601−1611.

(21) Honma, H.; Watanabe, H.; Kobayashi, T. *J. Electrochem. Soc.* **1994**, *141*, 1791−1795.

(22) Yin, X.; Hong, L.; Chen, B. H.; Ko, T. M. *J. Colloid Interface Sci.* **2003**, *262*, 89−96.

(23) Xiao, H.-M.; Fu, S.-Y.; Zhu, L.-P.; Li, Y.-Q.; Yang, G. *Eur. J. Inorg. Chem.* **2007**, *2007*, 1966−1971.

(24) Liang, H.; Xu, B.; Wang, Z. *Mater. Chem. Phys.* **2013**, *141*, 727−734.

(25) Trujillo, C.; Lamsabhi, A. M.; Mo, O.; Yanez, M. *Phys. Chem. Chem. Phys.* **2008**, *10*, 3229−3235.

(26) Chen, Z.; Dai, C.; Wu, G.; Nelson, M.; Hu, X.; Zhang, R.; Liu, J.; Xia, J. *Electrochim. Acta* **2010**, *55*, 8595−8599.

(27) Hernandez, J.; Wrschka, P.; Oehrlein, G. S. *J. Electrochem. Soc.* **2001**, *148*, G389−G397.

(28) Liu, Z.; Bai, H.; Xu, S.; Sun, D. D. *Int. J. Hydrogen Energy* **2011**, *36*, 13473−13480.

(29) Jana, S.; Das, S.; Das, N. S.; Chattopadhyay, K. K. *Mater. Res. Bull.* **2010**, *45*, 693−698.

(30) Devaraj, M.; Deivasigamani, R. K.; Jeyadevan, S. *Colloids Surf., B* **2013**, *102*, 554−561.

(31) Gao, X. P.; Bao, J. L.; Pa, G. L.; Zhu, H. Y.; Huang, P. X.; Wu, F.; Song, D. Y. *J. Phys. Chem. B* **2004**, *108*, 5547−5551.

(32) Martin, L.; Martinez, H.; Poinot, D.; Pecquenard, B.; Le Cras, F. *J. Phys. Chem. C* **2013**, *117*, 4421−4430.

(33) Dar, M. A.; Ahsanulhaq, Q.; Kim, Y. S.; Sohn, J. M.; Kim, W. B.; Shin, H. S. *Appl. Surf. Sci.* **2009**, *255*, 6279−6284.

(34) Li, F.; Liu, X.; Zhang, Q.; Kong, T.; Jin, H. *Cryst. Res. Technol.* **2012**, *47*, 1140−1147.

(35) Poizot, P.; Laruelle, S.; Grugeon, S.; Dupont, L.; Tarascon, J.-M. *Nature* **2000**, *407*, 496−499.

(36) Grugeon, S.; Laruelle, S.; Herrera-Urbina, R.; Dupont, L.; Poizot, P.; Tarascon, J. M. *J. Electrochem. Soc.* **2001**, *148*, A285.

(37) Xiang, J. Y.; Tu, J. P.; Zhang, L.; Zhou, Y.; Wang, X. L.; Shi, S. J. *Electrochim. Acta* **2010**, *55*, 1820−1824.

(38) Ni, S.; Lv, X.; Li, T.; Yang, X.; Zhang, L.; Ren, Y. *Electrochim. Acta* **2013**, *96*, 253−260.

(39) Koo, B.; Kim, H.; Cho, Y.; Lee, K. T.; Choi, N. S.; Cho, J. *Angew. Chem., Int. Ed.* **2012**, *51*, 8762−8767.

(40) Liu, R.; Li, D.; Tian, D.; Xia, G.; Wang, C.; Xiao, N.; Li, N.; Mack, N. H.; Li, Q.; Wu, G. *J. Power Sources* **2014**, *251*, 279−286.

(41) Mai, Y. J.; Wang, X. L.; Xiang, J. Y.; Qiao, Y. Q.; Zhang, D.; Gu, C. D.; Tu, J. P. *Electrochim. Acta* **2011**, *56*, 2306−2311.

(42) Rai, A. K.; Anh, L. T.; Gim, J.; Mathew, V.; Kang, J.; Paul, B. J.; Singh, N. K.; Song, J.; Kim, J. *J. Power Sources* **2013**, *244*, 435−441.

(43) Wang, F.; Tao, W.; Zhao, M.; Xu, M.; Yang, S.; Sun, Z.; Wang, L.; Song, X. *J. Alloys Compd.* **2011**, *509*, 9798−9803.

(44) Pan, Q.; Huang, K.; Ni, S.; Yang, F.; Lin, S.; He, D. *J. Alloys Compd.* **2009**, *484*, 322−326.

(45) Shaju, K. M.; Jiao, F.; Debart, A.; Bruce, P. G. *Phys. Chem. Chem. Phys.* **2007**, *9*, 1837−1842.